Photocarrier Dynamics in $MoTe_2$ Nanofilms with 2*H* and Distorted 1*T* Lattice Structures

Xiuxiu Han,[a] Xingyao Liang,[b] Dawei He,[,a] Liying Jiao,[b] Yongsheng Wang,[*,a] and Hui Zhao[*,c]*

[a]Key Laboratory of Luminescence and Optical Information, Ministry of Education, Institute of Optoelectronic Technology, Beijing Jiaotong University, Beijing 100044, China

[b]Key Laboratory of Organic Optoelectronics and Molecular Engineering of the Ministry of Education, Department of Chemistry, Tsinghua University, Beijing 100084, China

[c]Department of Physics and Astronomy, The University of Kansas, Lawrence, Kansas 66045, United States

E-mail: dwhe@bjtu.edu.cn; yshwang@bjtu.edu.cn; huizhao@ku.edu

ABSTRACT

Molybdenum telluride ($MoTe_2$), an emerging layered two-dimensional (2D) material, possesses excellent phase-changing properties. Previous studies revealed its reversible transition between 2*H* and 1*T*′ phases with a transition energy as small as 35 meV. Since 1*T*′-$MoTe_2$ is metallic, it can serve as an electrical contact for the semiconducting 2*H*

$MoTe_2$-based optoelectronic devices. Here, photocarrier dynamics in $MoTe_2$ nanofilms synthesized by a one-step method and with coexisting multiple phases are investigated by transient absorption measurements. Both the energy relaxation time and the recombination lifetime of the excitons are shorter in the 1*T*′-$MoTe_2$ compared to its 2*H* phase. These results provide information on the different photocarrier dynamical properties of these two phases, which is important for future 2D optoelectronic and phase-change electronic devices based on $MoTe_2$.

KEYWORDS: Molybdenum telluride ($MoTe_2$), multiple phases, photocarrier dynamics, transient absorption, the energy relaxation time, the recombination lifetime

INTRODUCTION

Two-dimensional (2D) materials are a new form of nanomaterials [1-2] with many potential applications such as transistors [3-5], ultrathin flexible electronic devices [6-7], photodetectors [8], photovoltaics [9-10], and superconducting devices[11]. For example, several transition metal dichalcogenides (TMDs) have sizeable and thickness-dependent bandgaps, resulting in thickness-tunable electronic and optical properties [3, 12-13]. One intriguing aspect of TMDs is that they can exhibit multiple crystalline phases [14] and thus possess different structural, symmetric, and physical properties [15-16]. For example, TMDs in hexagonal (*H*) phase are usually semiconducting, while those in 1*T* (octahedral structure) and 1*T*′ phases (distorted octahedral structure) are metallic [17-22]. This feature provides opportunities to form high-

quality metal-semiconductor homojunctions for various device applications.

Molybdenum telluride possesses a band gap close to that of silicon and has shown high homojunction efficiencies [23-25]. It exhibits two polymorphs, 2*H* and 1 *T′*, arising from the spatial arrangement of the Te atoms [16, 26]. The band gap of bulk 2*H*-$MoTe_2$ is indirect [27], however, its monolayer becomes a direct-band-gap semiconductor [28]. The infrared band gap and several other novel properties, such as strong spin-orbit coupling [5], tunable valley degeneracy splitting [29], and good thermoelectric properties [30], make 2*H*-$MoTe_2$ promising for various applications[27]. The metallic 1*T′*-$MoTe_2$ possesses in-plane anisotropy due to its distorted lattice [31], which are attractive for polarization-sensitive detectors [32], polarized surface plasmonics, and nonlinear optics devices [33]. In addition, 1*T′*-$MoTe_2$ has also shown sizable magnetic control of electrical resistance [26], strain-controlled superconductivity [34-35], as well as feasibility for phase engineering [16, 23]. Unlike MoS_2, which has a large phase transition energy of 0.8 eV [16], the transition energy of 2*H* and 1*T′* phases of $MoTe_2$ is as low as 35 meV [23]. It has been shown that such reversible phase transition [26] can be achieved by light [23], pressure [36], charge doping [16], and growth method [37]. Hence, 1*T′*-$MoTe_2$ can provide electrical contact to 2*H* $MoTe_2$ in various devices [23] and as a phase engineered material [15].

Recently, photocarrier and lattice dynamics in 2*H* semiconducting $MoTe_2$ nanofilms have been measured by several groups by using time-resolved spectroscopic techniques [38-43]. However, $MoTe_2$ nanofilm with 1*T′* phase have been less studied, especially in

comparison with its 2*H* counterpart. Here, photocarrier dynamics in 2*H*- and 1*T*′-$MoTe_2$ nanofilms are directly compared. Recently, time-resolved optical techniques, including transient absorption [44-46], time-resolved photoluminescence [47-50], and transient THz spectroscopy [51-53], have been successfully applied to study photocarrier dynamics in 2D materials. Carrier thermalization, hot carrier dynamics, exciton formation, transport, and recombination, as well as coherence carrier processes in a number of 2D materials have been revealed [54]. In this work, ultrafast pump-probe measurements are performed to study the photocarrier dynamics in $MoTe_2$ nanofilms with both 2*H* and 1*T*' regions. Rich dynamical features and significant difference were obtained from the two phase regions. Both the energy relaxation time and the exciton recombination lifetime are shorter in the 1*T*′-$MoTe_2$ compared to the 2*H* phase.

RESULTS AND DISCUSSION

The sample studied is displayed in Figure 1(a), which contains regions of both phases. Micro-Raman measurement with 532-nm excitation was performed, as shown in Figure 1(b). The spectrum from the central region shows three dominant modes that are consistent with previously reported A_{1g} (~174 cm^{-1}), E^1_{2g} (~235 cm^{-1}), and B^1_{2g} (~291 cm^{-1}) modes of 2*H*-$MoTe_2$ monolayers [55-56]. The Raman spectrum from the region labeled 1*T*′ is significantly different from that of the 2*H* region. As shown in Figure 1(b), rich

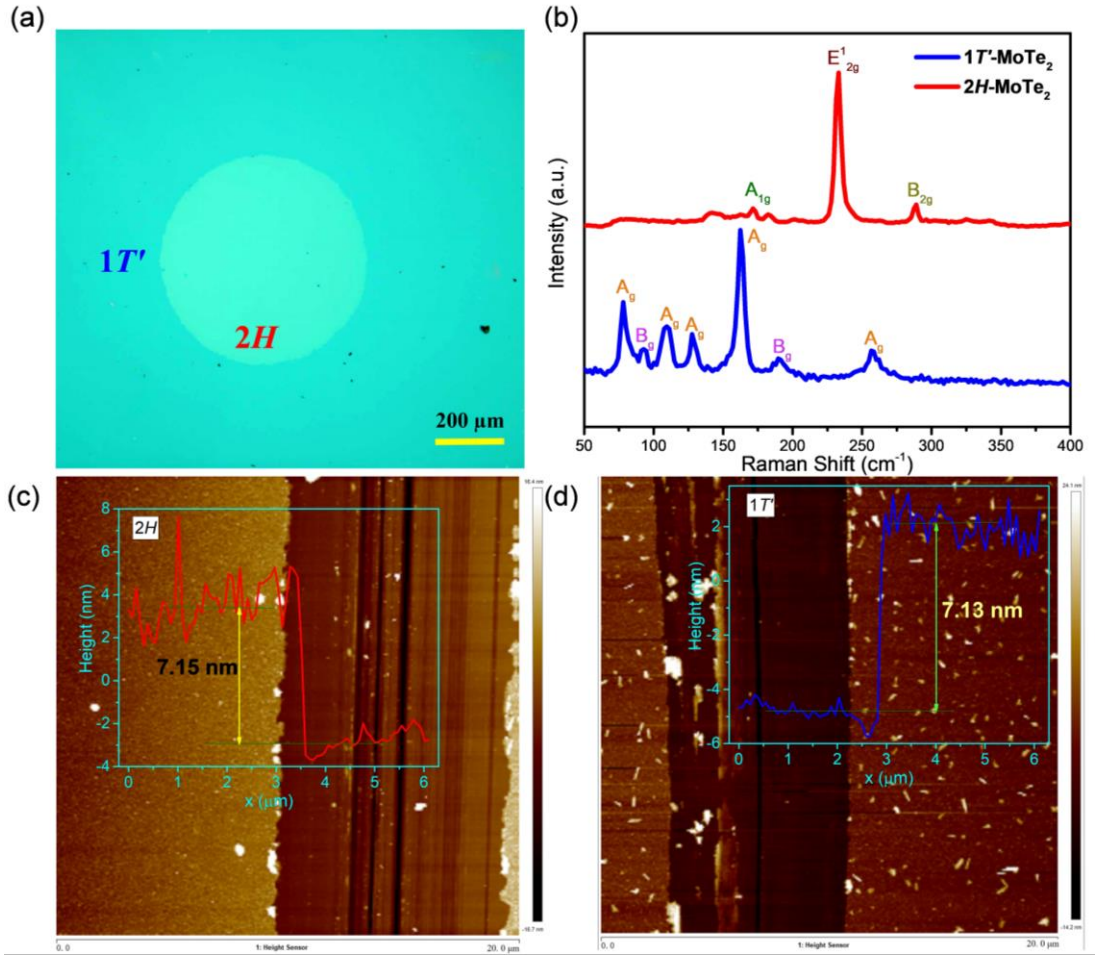

Figure 1. (a) A $MoTe_2$ nanofilm with two phases. (b) Raman spectra of the different regions shown in (a). (c) and (d) are AFM images of the sample containing the two phases. The insets are the corresponding AFM height profiles.

features are observed in the range between 50 and 400 cm^{-1}, which are consistent with previously assigned Raman peaks of 1*T*′-$MoTe_2$, such as the A_g (78 cm^{-1}), B_g (93 cm^{-1}), A_g (110 and ~128 cm^{-1}), A_g (162 cm^{-1}), B_g (189 cm^{-1}), and A_g (258 cm^{-1}) modes, based on previous experimental [57] and theoretical works [58]. Figure 1(c)-1(d) show the atomic force microscopic (AFM) images of different regions of the nanofilm. The cross-section

profiles show the thickness of different regions. For the 2*H* region, the thickness of is 7.15 nm, corresponding to 10 layers [59], while the thickness of 1*T*′-$MoTe_2$ is 7.13 nm, corresponding to 10 layers, too [33]. Hence, these Raman and AFM measurements establish that the sample contains two phases of 10-layer $MoTe_2$.

Figure 2(a)-2(b) shows the differential reflectance measured from the 2*H*-$MoTe_2$ region. A pump pulse of 670 nm and 100 fs injects photocarriers in the sample. Differential reflectance of an 820-nm probe pulse is measured. The pump, with a large photon energy of 1.85 eV, injects hot carriers. We note that the probe wavelength of 820 nm is chosen for experimental convenience, as it is directly obtained from the output of the Ti:sapphire oscillator. In Figure 2, curves with different colors show results with different pump fluences. To better compare the signal from different pump fluences, Figures 2(c) and 2(d) show the same data that are normalized (according to the value at 25 ps). The observed dynamics shows rich features: First, there is a narrow peak at zero probe delay. Second, there is a rising process of the signal for several picoseconds after the narrow peak. Third, the long-term decay of the signal persists for over 1 ns. On the fluence dependence, we observed two regimes. Above 100 μJ cm^{-2},

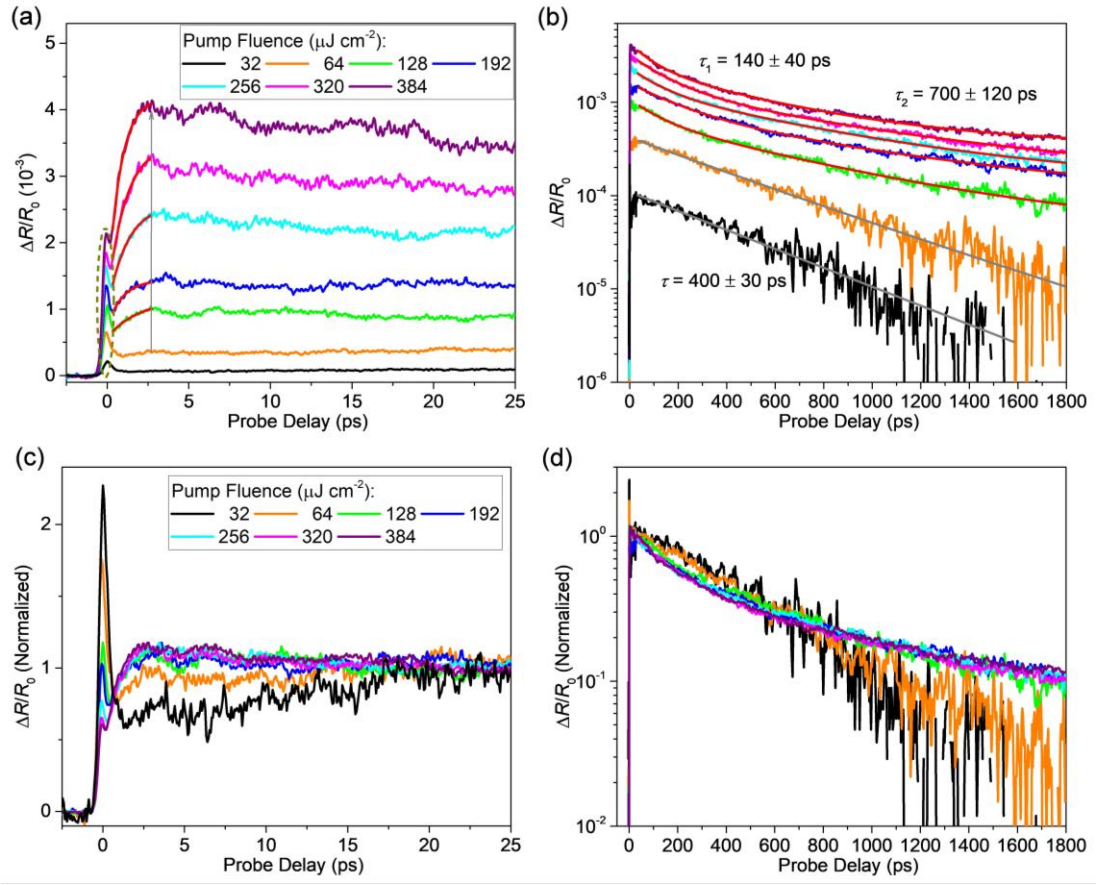

Figure 2. Photocarrier dynamics in 2*H*-$MoTe_2$. (a) an (b) are differential reflectance measured with an 820-nm probe and a 670-nm pump with fluences of 32, 64, 128, 192, 256, 320, and 380 μJ cm^{-2}, respectively. (c) and (d) show the same data as (a) and (b), respectively, but with the signal normalized for comparison.

the dynamics is independent of the fluence, as illustrated in (c) and (d). With lower fluences, however, the rise and the decay of the signal are both different from the high-fluence regime.

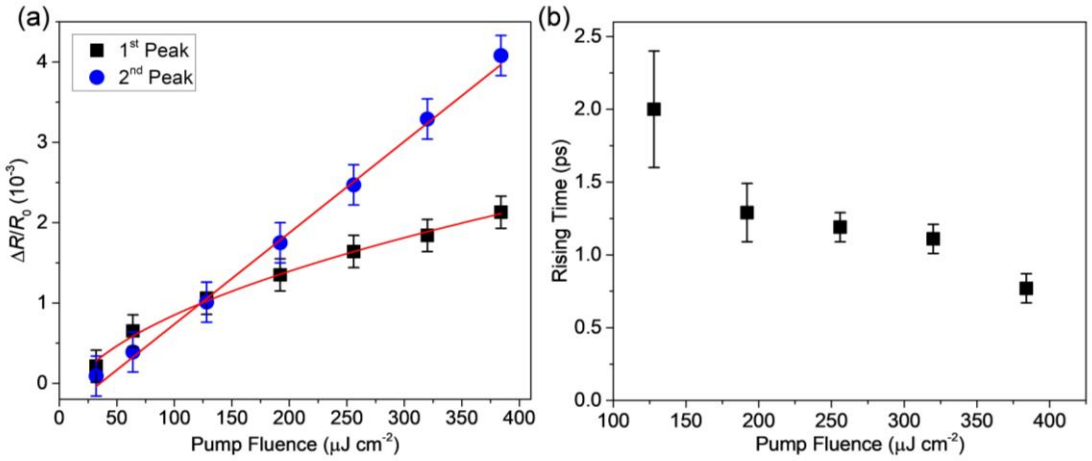

Figure 3. (a) The peak differential reflectance at zero delay (black squares) and the second peak at about 2 ps (blue circles) measured from the 2*H*-$MoTe_2$ sample. (b) The rising time deduced from Figure 2 (a).

To analyze these results, we first plot the heights of the narrow peak and the second peak [indicated in Figure 2(a) by the dashed ellipse and vertical arrow, respectively] against the pump fluence in Figure 3(a). The two peaks can be fit by square-root and linear functions of the fluence, respectively, as shown by the curves. The square-root dependence of the narrow peak indicates that its origin is unlikely related to the photocarriers. Since the electric field amplitude of the pump pulse scales as the square root of its intensity (and thus the fluence), this peak is proportional to the electric field amplitude of the pump. This suggests that it originates from nonlinear mixing of the two pulses involving direct exchange of their energy. The linear dependence of the second peak (and the rest of the signal) on the fluence shows that the signal is linear with the photocarrier density.

After the carrier-unrelated narrow peak, the rest of the signal reveals the dynamics of the photocarriers. We first focus on the high-fluence regime. The early rise of the

differential reflectance is described by $\Delta R/R_0 = C[1 - \exp(-t/\tau_r)]$, as shown by the red curves in Figure 2 (a). The fit rise time, τ_r is shown in Figure 3 (b), which decreases slightly from about 2 to about 1 ps as the pump fluence is increased. The long-term decay of the signal is fit by $\Delta R/R_0 = A_1 \exp(-t/\tau_1) + A_2 \exp(-t/\tau_2) + B$. The deduced time constants show no systematical dependence on the fluence, as expected since all the curves overlap after being normalized [Figure 2(d)]. By taking the averages, we obtained $\tau_1 = 140 \pm 40$ ps and $\tau_2 = 700 \pm 120$ ps.

To understand the physical origins of these transient processes, we recall that 2*H*-$MoTe_2$ has indirect and direct bandgaps of 0.88 and 1.02 eV at room temperature, respectively [27-28]. The 1.85-eV pump injects hot electron and hole pairs with excess energies on the order of 500 meV. The 1.51-eV probe couples to energy states that are about 200 - 300 meV above the band extremes. Hence, we can assume that the signal scales with the density of photocarriers in these high-energy states. Initially, the pump-injected photocarriers have narrow Gaussian energy distributions, with a width of about 10 meV (the spectral width of the pump pulse). These nonthermal and hot carriers will undergo a thermalization process, in which carriers exchange their kinetic energy and momentum by carrier-carrier scattering to establish Fermi-Dirac distributions. In this process, the occupation of the energy states being probed increases. Hence, we attribute the few-ps rise of the signal to this process. Since the intercarrier scattering rate increases with their density, the decrease of the rise time with the pump fluence is reasonable. Meanwhile, excitons are

also expected to form from the free electron-hole pairs on this time scale: Previous studies have revealed that in monolayer semiconductors, the exciton binding energies can reach several hundreds of meV [60-61], and electron-hole pairs can form excitons within 1 ps [62-64]. In the nanofilm studied here, we expect similarly large exciton binding energies. Hence, the electron-hole pairs can form hot excitons in this few-ps time range. After these processes, the carrier system is composed of hot excitons. The energy relaxation, or cooling, of the hot excitons from high energy states to the band extremes drives the carriers out of the probed states. We assign the 140-ps process to this mechanism. Finally, cooled excitons recombine, returning the system to the pre-pump condition. The 700-ps process is thus attributed to the exciton recombination. In the high pump fluence regime, the two decay time constants are both fluence independent, suggesting that the exciton-exciton annihilation, which often dominates exciton dynamics in monolayer semiconductors [65-66], plays an insignificant role here. Otherwise, the time constants would have decreased significantly with increasing the fluence.

We now discuss the results with low pump fluences. As shown in Figure 2, the signal rise is significantly slower with low injected carrier densities. The overall signal decay is faster than the high-density results, and can be described by an exponential decay function of $\tau = 400 \pm 30$ ps. At low injected densities, trapping of carriers by defect states can significantly influence the carrier dynamics. The 400-ps decay in this regime is assigned to defect-assisted carrier trapping or recombination.

To reveal the effect of the crystalline phase on the photocarrier dynamics, we repeated the transient absorption measurements on the $1T'$ region of the $MoTe_2$ nanofilm sample under the same experimental conditions. Figure 4 summarizes the key results. On the short time range [Figure 4(a)], we observe a pronounced oscillatory component that follows the initial narrow peak, which superimposes to the slow-decaying signal. We note that this component also appears in the $2H$ region, shown in Figure 2(a). However, it was less pronounced due to the larger overall signal in the $2H$ region (by about a factor of 4). According to Figure 4(c), the signal is pump-fluence-independent. By fitting this oscillatory component with a dumped sinusoidal expression, $A\exp(-t/\tau_s)\sin(2\pi t/\mathrm{T} + t_0)$ [red curves in Figure 4(a)], we deduced the period of $\mathrm{T} = 4.16 \pm 0.12$ ps and the decay constant of 5.0 ± 0.9 ps. We attributed this component is to the coherence lattice vibration excited by the pump pulse.

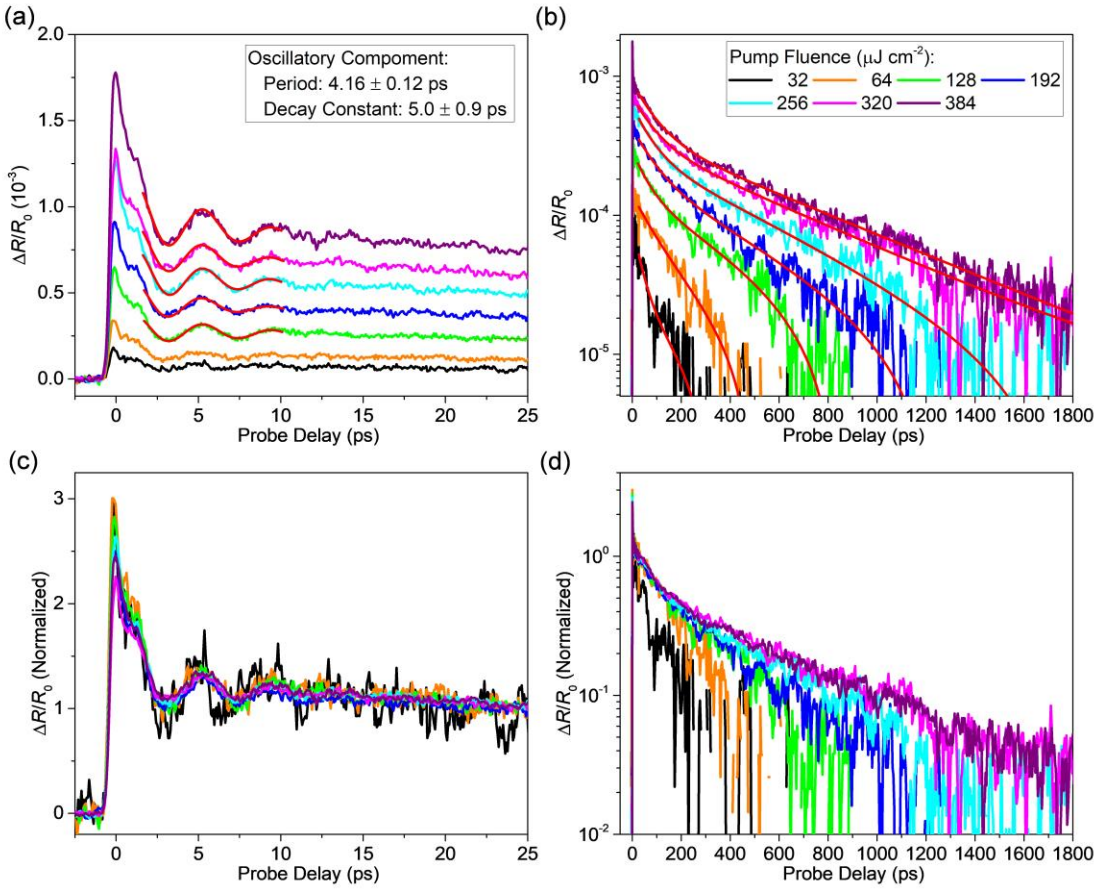

Figure 4. Photocarrier dynamics in 1T'-$MoTe_2$. (a) Differential reflectance with an 820-nm probe and a 670-nm pump of 32, 64, 128, 192, 256, 320, and 380 μJ cm^{-2}, respectively. The red curves are fits to the oscillatory component (see text). (b) Same as (a) with the red curves as double exponential fits. (c) and (d) are same as (a) and (b), respectively, but with data normalized for comparison.

Figure 5(a) shows the peak differential reflectance at zero delay (black squares) and that at 25 ps (blue circles) against the pump fluence. The signal at 25 ps was selected as an example of the early signal magnitude. It approximately scales with the pump fluence, as confirmed by a power fit of AF^b, which yielded a power of $b = 1.03 \pm 0.03$. The dependence of the peak height at zero delay, however, is neither linear nor square root of

the pump fluence. By using the power fit, we found a power of 0.87 ± 0.05. This indicates that the peak height has contributions from both nonlinear optical interactions of the two pulses and the lattice oscillation. Finally, the decay of the signal, shown in Figure 4(b), is fit by the double exponential function. As summarized in Figure 5(b), the short time constant is about 80 ps and is fluence independent, while the long-time constant is in the range of 480 - 580 ps and slightly increases with the fluence. These results show that the energy relaxation and the recombination lifetime of the excitons are shorter in the 1*T*′-$MoTe_2$ compared to the 2*H* phase.

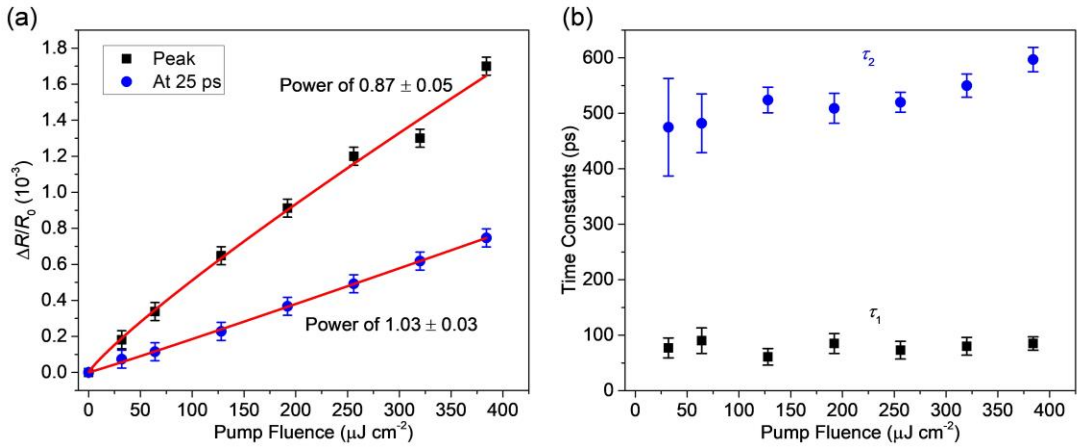

Figure 5. (a) The peak signal at zero delay (black squares) and the signal at 25 ps (blue circles) measured from the 1*T*′-$MoTe_2$ sample. The red lines are power fits with the power indicated in the figure. (b) The decay time constants by the fits shown in Figure 3(a).

CONCLUSION

Transient absorption measurements are performed on $MoTe_2$ nanofilms with 2*H*- and 1*T*′ regions. Coherent lattice vibration is observed in both phases. By time resolving the

photocarrier dynamics, we deduce an energy relaxation time of 140 ps and exciton lifetime of 700 ps in 2*H*-$MoTe_2$. In 1*T*'-$MoTe_2$, both time constants are shorter (80 ps and 500 ps, respectively). These parameters are useful for understanding carrier dynamics in these materials and modeling device performances based on these materials. For example, the energy relaxation time provides a limit on devices utilizing hot-carrier effects. The exciton lifetime is closely related to both the device operation speed and the energy conversion efficiency. Hence, this work provides quantitative parameters describing the dynamical properties of $MoTe_2$ with both semiconducting and metallic phases, and offers insights into $MoTe_2$ for future 2D optoelectronic and phase-change electronic devices with an ohmic contact. Especially, the results provide basic support for 1*T*′-$MoTe_2$ as the contact material of 2*H*- $MoTe_2$ in future, and are beneficial for $MoTe_2$, as a promising phase engineering material to be widely applicated.

EXPERIMENTAL SECTION

Sample Synthesis. $MoTe_2$ nanofilms of 2*H* and 1*T*′ phases were prepared by one-step chemical vapor deposition (CVD). Under ambient conditions, two 1 nm Mo films, which were obtained by magnetron sputtering, were put in a ceramic crucible with a "face-to-face" structure. The Te powders was covered and loaded to the crucible downstream. Before the growth, molecular sieves were set in the crucible. To synthesize $MoTe_2$ films with both phases, the crucible was heated to 690 ℃ from room temperature in 15 min under flowing

the 25 sccm gas mixture of Ar/H_2 construction for 95%/5%. After 90 min, the furnace was powered off and cooled down to room temperature naturally.

Transient Absorption Measurement. An Ti:sapphire laser produces 100-fs and 820-nm pulses every 13 ns. This output pumps an optical parametric oscillator to generate a 670-nm signal pulse, serving as the pump pulse. The rest of the 820-nm pulse serves as the probe. The two pulses are combined and co-focused to the sample by an objective lens (numerical aperture: 0.4). The spot size is about 1.5 μm. The probe reflection is sent to a photodiode and measured by a lock-in amplifier. The differential reflectance is defined as $\Delta R/R_0 = (R - R_0)/R_0$, where R and R_0 are the reflectance of the sample when the pump beam is unblocked and blocked, respectively. All the measurements were performed at room temperature with samples exposed to air.

AUTHOR INFORMATION

Corresponding Author

Dawei He - *Key Laboratory of Luminescence and Optical Information, Ministry of Education, Institute of Optoelectronic Technology, Beijing Jiaotong University, Beijing 100044, China*; Email: dwhe@bjtu.edu.cn

Yongsheng Wang - *Key Laboratory of Luminescence and Optical Information, Ministry of Education, Institute of Optoelectronic Technology, Beijing Jiaotong University, Beijing 100044, China*; Email: yshwang@bjtu.edu.cn

Hui Zhao - *Department of Physics and Astronomy, The University of Kansas, Lawrence,*

Kansas 66045, United States； Email: huizhao@ku.edu

Authors

Xiuxiu Han - *Key Laboratory of Luminescence and Optical Information, Ministry of Education, Institute of Optoelectronic Technology, Beijing Jiaotong University, Beijing 100044, China*； Email: 18118028@bjtu.edu.cn

Xingyao Liang - *Key Laboratory of Organic Optoelectronics and Molecular Engineering of the Ministry of Education, Department of Chemistry, Tsinghua University, Beijing 100084, China*； Email: xingyao92@qq.com

Liying Jiao - *Key Laboratory of Organic Optoelectronics and Molecular Engineering of the Ministry of Education, Department of Chemistry, Tsinghua University, Beijing 100084, China*； Email: lyjiao@mail.tsinghua.edu.cn

Notes

The authors declare no competing financial interest.

ACKNOWLEDGEMENTS

Y.W. and D.H. are grateful for the financial support of National Natural Science Foundation of China (61875236, 61905010, 61975007), Beijing Natural Science Foundation (Z190006). H.Z. was supported by the U.S. Department of Energy, Office of Basic Energy Sciences, Division of Materials Sciences and Engineering under Award DE-SC0020995.

REFERENCE

(1). Novoselov, K. S.; Geim, A. K.; Morozov, S. V.; Jiang, D.; Zhang, Y.; Dubonos, S. V.; Grigorieva, I. V.; Firsov, A. A. Electric Field Effect in Atomically Thin Carbon Films. *Science* **2004**, *306*, 666-669.

(2). Geim, A. K.; Novoselov, K. S., The rise of graphene. *Nature Materials* **2007**, *6*, 183-191.

(3). Radisavljevic, B.; Radenovic, A.; Brivio, J.; Giacometti, V.; Kis, A. Single-layer MoS_2 transistors. *Nature nanotechnology* **2011**, *6*, 147-50.

(4). Lin, Y. F.; Xu, Y.; Wang, S. T.; Li, S. L.; Yamamoto, M.; Aparecido-Ferreira, A.; Li, W.; Sun, H.; Nakaharai, S.; Jian, W. B.; Ueno, K.; Tsukagoshi, K. Ambipolar $MoTe_2$ transistors and their applications in logic circuits. *Advanced materials* **2014**, *26*, 3263-9.

(5). Pradhan, N. R.; Rhodes, D.; Feng, S.; Xin, Y.; Memaran, S.; Moon, B. H.; Terrones, H.; Terrones, M.; Balicas, L. Field-Effect Transistors Based on Few-Layered α-$MoTe_2$. *ACS Nano* **2014**, *8*, 5911-5920.

(6). Choi, M. S.; Lee, G. H.; Yu, Y. J.; Lee, D. Y.; Lee, S. H.; Kim, P.; Hone, J.; Yoo, W. J. Controlled charge trapping by molybdenum disulphide and graphene in ultrathin heterostructured memory devices. *Nature communications* **2013**, *4*, 1624.

(7). Bertolazzi, S.; Brivio, J.; Kis, A. Stretching and Breaking of Ultrathin MoS_2. *ACS Nano* **2011**, *5*, 9703-9709.

(8). Zhang, W.; Chuu, C. P.; Huang, J. K.; Chen, C. H.; Tsai, M. L.; Chang, Y. H.; Liang, C. T.; Chen, Y. Z.; Chueh, Y. L.; He, J. H.; Chou, M. Y.; Li, L. J. Ultrahigh-gain

photodetectors based on atomically thin graphene-MoS_2 heterostructures. *Scientific reports* **2014**, *4*, 3826.

(9). Bernardi, M.; Palummo, M.; Grossman, J. C. Extraordinary sunlight absorption and one nanometer thick photovoltaics using two-dimensional monolayer materials. *Nano letters* **2013**, *13*, 3664-70.

(10). Gan, L. Y.; Zhang, Q.; Cheng, Y.; Schwingenschlogl, U. Photovoltaic Heterojunctions of Fullerenes with MoS_2 and WS_2 Monolayers. *Journal of Physical Chemistry Letters* **2014**, *5*, 1445-9.

(11). Ye, J. T. ; Zhang,Y. J.; Akashi,R.; Bahramy, M. S.; Arita, R.;Iwasa, Y. Superconducting Dome in a Gate-Tuned Band Insulator. *Science* **2012**, *338*, 1193-1196.

(12). Kumar, A.; Ahluwalia, P. K. Electronic structure of transition metal dichalcogenides monolayers 1H-MX2 (M = Mo, W; X = S, Se, Te) from ab-initio theory: new direct band gap semiconductors. *The European Physical Journal B* **2012**, *85*.

(13). Mak, K. F.; Lee, C.; Hone, J.; Shan, J.; Heinz, T. F. Atomically thin MoS(2): a new direct-gap semiconductor. *Physical review letters* **2010**, *105*, 136805.

(14). Manzeli, S.; Ovchinnikov, D.; Pasquier, D.; Yazyev, O. V.; Kis, A., 2D transition metal dichalcogenides. *Nature Reviews Materials* **2017**, *2*.

(15). Tan, Y.; Luo, F.; Zhu, M.; Xu, X.; Ye, Y.; Li, B.; Wang, G.; Luo, W.; Zheng, X.; Wu, N.; Yu, Y.; Qin, S.; Zhang, X. A. Controllable 2H-to-1T' phase transition in few-layer $MoTe_2$. *Nanoscale* **2018**, *10*, 19964-19971.

(16). Duerloo, K. A.; Li, Y.; Reed, E. J. Structural phase transitions in two-dimensional Mo- and W-dichalcogenide monolayers. *Nature communications* **2014**, *5*, 4214.

(17). Yang, H.; Kim, S. W.; Chhowalla, M.; Lee, Y. H. Structural and quantum-state phase transitions in van der Waals layered materials. *Nature Physics* **2017**, *13*, 931-937.

(18). Kan, M.; Wang, J. Y.; Li, X. W.; Zhang, S. H.; Li, Y. W.; Kawazoe, Y.; Sun, Q.; Jena, P. Structures and Phase Transition of a MoS_2 Monolayer. *The Journal of Physical Chemistry C* **2014**, *118*, 1515-1522.

(19). Kappera, R.; Voiry, D.; Yalcin, S. E.; Branch, B.; Gupta, G.; Mohite, A. D.; Chhowalla, M. Phase-engineered low-resistance contacts for ultrathin MoS_2 transistors. *Nature Materials* **2014**, *13*, 1128-34.

(20). Wang, L.; Xu, Z.; Wang, W.; Bai, X. Atomic mechanism of dynamic electrochemical lithiation processes of MoS(2) nanosheets. *Journal of the American Chemical Society* **2014**, *136*, 6693-7.

(21). Lin, Y. C.; Dumcenco, D. O.; Huang, Y. S.; Suenaga, K. Atomic mechanism of the semiconducting-to-metallic phase transition in single-layered MoS_2. *Nature nanotechnology* **2014**, *9*, 391-6.

(22). Zhu, J.; Wang, Z.; Yu, H.; Li, N.; Zhang, J.; Meng, J.; Liao, M.; Zhao, J.; Lu, X.; Du, L.; Yang, R.; Shi, D.; Jiang, Y.; Zhang, G. Argon Plasma Induced Phase Transition in Monolayer MoS_2. *Journal of the American Chemical Society* **2017**, *139*, 10216-10219.

(23). Cho, S.; Kim, S.; Kim, J. H.; Zhao, J.; Seok, J.; Keum, D. H.; Baik, J.; Choe, H.;

Chang, K. J.; Suenaga, K.; Kim,S. W.; Lee, Y. H.; Yang, H. Phase patterning for ohmic homojunction contact in $MoTe_2$. *Science* **2015**, *349*, 625-628.

(24). Ma, R.; Zhang, H.; Yoo, Y.; Degregorio, Z. P.; Jin, L.; Golani, P.; Ghasemi Azadani, J.; Low, T.; Johns, J. E.; Bendersky, L. A.; Davydov, A. V.; Koester, S. J. $MoTe_2$ Lateral Homojunction Field-Effect Transistors Fabricated using Flux-Controlled Phase Engineering. *ACS Nano* **2019**, *13*, 8035-8046.

(25). Xu, X.; Pan, Y.; Liu, S.; Han, B.; Gu, P.; Li, S.; Xu, W.; Peng, Y.; Han, Z.; Chen, J.;Gao, P.; Ye, Y. Seeded 2D epitaxy of large-area single-crystal films of the van der Waals semiconductor 2H $MoTe_2$. *Science* **2021**, *372*, 195-200.

(26). Keum, D. H.; Cho, S.; Kim, J. H.; Choe, D.-H.; Sung, H.-J.; Kan, M.; Kang, H.; Hwang, J.-Y.; Kim, S. W.; Yang, H.; Chang, K. J.; Lee, Y. H. Bandgap opening in few-layered monoclinic $MoTe_2$. *Nature Physics* **2015**, *11*, 482-486.

(27). Grant, A. J.; Griffiths, T. M.; Pitt, G. D.; Yoffe, A. D. The electrical properties and the magnitude of the indirect gap in the semiconducting transition metal dichalcogenide layer crystals. *Journal of Physics C: Solid State Physics* **1795**, *8*, L17.

(28). Ruppert, C.; Aslan, O. B.; Heinz, T. F. Optical properties and band gap of single- and few-layer $MoTe_2$ crystals. *Nano letters* **2014**, *14*, 6231-6.

(29). Qi, J.; Li, X.; Niu, Q.; Feng, J. Giant and tunable valley degeneracy splitting in $MoTe_2$. *Physical Review B* **2015**, *92*.

(30). Balendhran, S.; Walia, S.; Nili, H.; Ou, J. Z.; Zhuiykov, S.; Kaner, R. B.; Sriram, S.;

Bhaskaran, M.; Kalantar-zadeh, K. Two-Dimensional Molybdenum Trioxide and Dichalcogenides. *Advanced Functional Materials* **2013**, *23*, 3952-3970.

(31). Gong, C.; Zhang, Y.; Chen, W.; Chu, J.; Lei, T.; Pu, J.; Dai, L.; Wu, C.; Cheng, Y.; Zhai, T.; Li, L.; Xiong, J. Electronic and Optoelectronic Applications Based on 2D Novel Anisotropic Transition Metal Dichalcogenides. *Advanced science* **2017**, *4,* 1700231.

(32). Lai, J.; Liu, X.; Ma, J.; Wang, Q.; Zhang, K.; Ren, X.; Liu, Y.; Gu, Q.; Zhuo, X.; Lu, W.; Wu, Y.; Li, Y.; Feng, J.; Zhou, S.; Chen, J. H.; Sun, D. Anisotropic Broadband Photoresponse of Layered Type-II Weyl Semimetal $MoTe_2$. *Advanced materials* **2018**, *30*, e1707152.

(33). Zhu, M.; Zhao, Y.; Feng, Q.; Lu, H.; Zhang, S.; Zhang, N.; Ma, C.; Li, J.; Zheng, J.; Zhang, J.; Xu, H.; Zhai, T.; Zhao, J. Linear Dichroism and Nondestructive Crystalline Identification of Anisotropic Semimetal Few-Layer $MoTe_2$. *Small* **2019**, *15*, e1903159.

(34). Qi, Y.; Naumov, P. G.; Ali, M. N.; Rajamathi, C. R.; Schnelle, W.; Barkalov, O.; Hanfland, M.; Wu, S. C.; Shekhar, C.; Sun, Y.; Suss, V.; Schmidt, M.; Schwarz, U.; Pippel, E.; Werner, P.; Hillebrand, R.; Forster, T.; Kampert, E.; Parkin, S.; Cava, R. J.; Felser, C.; Yan, B.; Medvedev, S. A. Superconductivity in Weyl semimetal candidate $MoTe_2$. *Nature communications* **2016**, *7*, 11038.

(35). Zhou, J.; Liu, F.; Lin, J.; Huang, X.; Xia, J.; Zhang, B.; Zeng, Q.; Wang, H.; Zhu, C.; Niu, L.; Wang, X.; Fu, W.; Yu, P.; Chang, T. R.; Hsu, C. H.; Wu, D.; Jeng, H. T.; Huang, Y.; Lin, H.; Shen, Z.; Yang, C.; Lu, L.; Suenaga, K.; Zhou, W.; Pantelides, S. T.; Liu, G.; Liu,

Z. Large-Area and High-Quality 2D Transition Metal Telluride. *Advanced materials* **2017**, *29*.

(36). Song, S.; Keum, D. H.; Cho, S.; Perello, D.; Kim, Y.; Lee, Y. H. Room Temperature Semiconductor-Metal Transition of $MoTe_2$ Thin Films Engineered by Strain. *Nano letters* **2016**, *16*, 188-93.

(37). Empante, T. A.; Zhou, Y.; Klee, V.; Nguyen, A. E.; Lu, I. H.; Valentin, M. D.; Naghibi Alvillar, S. A.; Preciado, E.; Berges, A. J.; Merida, C. S.; Gomez, M.; Bobek, S.; Isarraraz, M.; Reed, E. J.; Bartels, L. Chemical Vapor Deposition Growth of Few-Layer $MoTe_2$ in the 2H, 1T', and 1T Phases: Tunable Properties of $MoTe_2$ Films. *ACS Nano* **2017**, *11*, 900-905.

(38) Krishnamoorthy, A.; Lin, M. F.; Zhang, X.; Weninger, C.; Ma, R.; Britz, A.; Tiwary, C. S.; Kochat, V.; Apte, A.; Yang, J.; Park, S.; Li, R.; Shen, X.; Wang, X.; Kalia, R.; Nakano, A.; Shimojo, F.; Fritz, D.; Bergmann, U.; Ajayan, P.; Vashishta, P. Optical Control of Non-Equilibrium Phonon Dynamics. *Nano letters* **2019**, *19*, 4981-4989.

(39) Bassman, L.; Krishnamoorthy, A.; Kumazoe, H.; Misawa, M.; Shimojo, F.; Kalia, R. K.; Nakano, A.; Vashishta, P. Electronic Origin of Optically-Induced Sub-Picosecond Lattice Dynamics in $MoSe_2$ Monolayer. *Nano letters* **2018**, *18*, 4653-4658.

(40) Pan, S.; Kong, W.; Liu, J.; Ge, X.; Zereshki, P.; Hao, S.; He, D.; Wang, Y.; Zhao, H. Understanding Spatiotemporal Photocarrier Dynamics in Monolayer and Bulk MoTe2 for Optimized Optoelectronic Devices. *ACS Applied Nano Materials* **2018**, *2*, 459-464.

(41) Kim, J. H.; Bergren, M. R.; Park, J. C.; Adhikari, S.; Lorke, M.; Frauenheim, T.; Choe, D. H.; Kim, B.; Choi, H.; Gregorkiewicz, T.; Lee, Y. H. Carrier multiplication in van der Waals layered transition metal dichalcogenides. *Nature communications* 2019, *10*, 5488.

(42) Bataller, A. W.; Younts, R. A.; Rustagi, A.; Yu, Y.; Ardekani, H.; Kemper, A.; Cao, L.; Gundogdu, K. Dense Electron-Hole Plasma Formation and Ultralong Charge Lifetime in Monolayer MoS2 via Material Tuning. *Nano letters* 2019, *19*, 1104-1111.

(43) Zhang, M. Y.; Wang, Z. X.; Li, Y. N.; Shi, L. Y.; Wu, D.; Lin, T.; Zhang, S. J.; Liu, Y. Q.; Liu, Q. M.; Wang, J.; Dong, T.; Wang, N. L. Light-Induced Subpicosecond Lattice Symmetry Switch in $MoTe_2$. *Physical Review X* 2019, *9,* 023016.

(44) Wang, R.; Ruzicka, B. A.; Kumar, N.; Bellus, M. Z.; Chiu, H. Y.; Zhao, H. Ultrafast and spatially resolved studies of charge carriers in atomically thin molybdenum disulfide. *Physical Review B* 2012, *86*, 045406.

(45) Zhu, C. R.; Zhang, K.; Glazov, M.; Urbaszek, B.; Amand, T.; Ji, Z. W.; Liu, B. L.; Marie, X. Exciton valley dynamics probed by Kerr rotation in WSe_2 monolayers. *Physical Review B* 2014, *90*, 161302.

(46) Wang, H.; Zhang, C.; Rana, F. Ultrafast dynamics of defect-assisted electron-hole recombination in monolayer MoS_2. *Nano letters* 2015, *15*, 339-45.

(47) Korn, T.; Heydrich, S.; Hirmer, M.; Schmutzler, J.; Schuller, C. Low-temperature photocarrier dynamics in monolayer MoS_2. *Applied Physics Letters* 2011, *9*, 102109.

(48) Lagarde, D.; Bouet, L.; Marie, X.; Zhu, C. R.; Liu, B. L.; Amand, T.; Tan, P. H.;

Urbaszek, B. Carrier and polarization dynamics in monolayer MoS_2. *Physical review letters* 2014, *112*, 047401.

(49) Wang, G.; Bouet, L.; Lagarde, D.; Vidal, M.; Balocchi, A.; Amand, T.; Marie, X.; Urbaszek, B. Valley dynamics probed through charged and neutral exciton emission in monolayerWSe_2. *Physical Review B* 2014, *90*, 075413.

(50) Wang, G.; Marie, X.; Bouet, L.; Vidal, M.; Balocchi, A.; Amand, T.; Lagarde, D.; Urbaszek, B. Exciton dynamics in WSe_2 bilayers. *Applied Physics Letters* 2014, *105*, 182105.

(51) Docherty C. J.; Parkinson P.; Joyce H. J.; Chiu M. H., Chen C. H.; Lee M. Y.; Li L. J.; Herz L. M.; Johnston M. B. Ultrafast Transient Terahertz Conductivity of Monolayer MoS_2 and WSe_2 Grown by Chemical Vapor Deposition. *ACS nano* 2014, *8*, 11147-11153.

(52) Strait, J. H.; Nene, P.; Rana, F. High intrinsic mobility and ultrafast carrier dynamics in multilayer metal-dichalcogenide MoS_2. *Physical Review B* 2014, *90*, 245402.

(53) Liu, X. F.; Yu, H. Y.; Ji, Q. Q.; Gao, Z. H.; Ge, S. F.; Qiu, J.; Liu, Z. F.; Zhang, Y. F.; Sun, D. An ultrafast terahertz probe of the transient evolution of the charged and neutral phase of photo-excited electron-hole gas in a monolayer semiconductor. *2D Materials* 2016, *3*, 014001.

(54) Ceballos, F.; Zhao, H. Ultrafast Laser Spectroscopy of Two-Dimensional Materials Beyond Graphene. *Advanced Functional Materials* 2016, *27*, 1604509,

(55). Zhang, H.; Zhou, W.; Li, X.; Xu, J.; Shi, Y.; Wang, B.; Miao, F. High temperature

Raman investigation of few-layer $MoTe_2$. *Applied Physics Letters* **2016**, *108*, 91902.

(56). Lezama, I. G.; Arora, A.; Ubaldini, A.; Barreteau, C.; Giannini, E.; Potemski, M.; Morpurgo, A. F. Indirect-to-direct band gap crossover in few-layer $MoTe_2$. *Nano letters* **2015**, *15*, 2336-2342.

(57). Zhou, L.; Zubair, A.; Wang, Z.; Zhang, X.; Ouyang, F.; Xu, K.; Fang, W.; Ueno, K.; Li, J.; Palacios, T.; Kong,J.; S. Dresselhaus, M. Synthesis of High-Quality Large-Area Homogenous 1T' $MoTe_2$ from Chemical Vapor Deposition. *Advanced materials* **2016**, *28*, 9526-9531.

(58). Kan, M.; Nam, H. G.; Lee, Y. H.; Sun, Q. Phase stability and Raman vibration of the molybdenum ditelluride ($MoTe_2$) monolayer. *Physical Chemistry Chemical Physics* **2015**, *17*, 14866-14871.

(59). Yamamoto, M.; Wang, S. T.; Ni, M.; Lin,Y.; Li, S.; Aikawa, S.; Jian, W.; Ueno, K.; Wakabayashi, K.; Tsukagoshi, K. Strong Enhancement of Raman Scattering from a Bulk-Inactive Vibrational Mode in Few-Layer $MoTe_2$. *ACS Nano* **2014**, *8*, 3895-903.

(60) He, K.; Kumar, N.; Zhao, L.; Wang, Z.; Mak, K. F.; Zhao, H.; Shan, J. Tightly bound excitons in monolayer WSe_2. *Physical review letters* **2014,** *113*, 026803.

(61) Chernikov, A.; Berkelbach, T. C.; Hill, H. M.; Rigosi, A.; Li, Y.; Aslan, O. B.; Reichman, D. R.; Hybertsen, M. S.; Heinz, T. F. Exciton binding energy and nonhydrogenic Rydberg series in monolayer WS_2. *Physical review letters* **2014,** *113*, 076802.

(62) Ceballos F.; Cui Q.; Bellusa M. Z.; Zhao H. Exciton Formation in Monolayer

Transition Metal Dichalcogenides. *Nanoscale* **2016,** *8*, 11681-11688.

(63) Steinleitner, P.; Merkl, P.; Nagler, P.; Mornhinweg, J.; Schuller, C.; Korn, T.; Chernikov, A.; Huber, R. Direct Observation of Ultrafast Exciton Formation in a Monolayer of WSe2. *Nano letters* **2017,** *17*, 1455-1460.

(64) Valencia-Acuna, P.; Zereshki, P.; Tavakoli, M. M.; Park, J. H.; Kong, J.; Zhao, H. Transient absorption of transition metal dichalcogenide monolayers studied by a photodope-pump-probe technique. *Physical Review B* **2020,** *102*, 035414.

(65) Kumar, N.; Cui, Q.; Ceballos, F.; He, D.; Wang, Y.; Zhao, H. Exciton-exciton annihilation in MoSe2monolayers. *Physical Review B* **2014,** *89*, 125427.

(66) Sun, D.; Rao, Y.; Reider, G. A.; Chen, G.; You, Y.; Brezin, L.; Harutyunyan, A. R.; Heinz, T. F. Observation of rapid exciton-exciton annihilation in monolayer molybdenum disulfide. *Nano letters* **2014,** *14*, 5625-5629.

TOC graph